

# Analysis of surface compositions in the Oxia Palus region on Mars from Mars Global Surveyor Thermal Emission Spectrometer Observations

Michael B. Wyatt

Department of Geological Sciences, Arizona State University, Tempe, Arizona, USA

Harry Y. McSween Jr. and Jeffrey E. Moersch

Department of Geological Sciences, University of Tennessee, Knoxville, Tennessee, USA

Phillip R. Christensen

Department of Geological Sciences, Arizona State University, Tempe, Arizona, USA

Received 30 September 2002; revised 19 March 2003; accepted 6 May 2003; published 13 September 2003.

[1] We examine the distribution of Thermal Emission Spectrometer (TES) derived surface compositions in the Oxia Palus region on Mars through high-spatial-resolution mapping and integration with Mars Orbiter Camera and Mars Orbiter Laser Altimeter data sets. We also fit the basalt and andesite-weathered basalt interpretations of TES surface type 1 and type 2 materials into multiple working hypotheses to describe the origin of surface compositions. A mixing/transition from surface type 1 to type 2 is observed in low-albedo regions of southern Acidalia Planitia and may represent either (1) an influx of basaltic sediment from the southern highlands, deposited on and mixed with andesitic volcanics; (2) an influx of water-transported basaltic sediment from the southern highlands that was altered and later deposited as a thin sedimentary veneer; or (3) different degrees of weathering of indigenous basalt, marking the geographic extent of submarine alteration of basaltic crust. TES spectra of low-albedo intracrater materials reveal that surface type 1 compositions form a central core on crater floors, while type 2 compositions form a surrounding arc on the dark downwind sides of crater walls. Intracrater floor materials are interpreted as eolian sediment, and wall materials are interpreted as either eolian sediment or eroded material from in-place crater wall lithologies. Surface type 1 and type 2 compositions are also observed in adjacent low-albedo wind streaks; however, a mixing trend is not as evident. The Mars Pathfinder landing site and Ares and Tiu Valles source regions are sufficiently blanketed by fine-grained dust to prohibit the analysis of surface rock compositions. *INDEX TERMS*: 6225 Planetology: Solar System Objects: Mars; 5470 Planetology: Solid Surface Planets: Surface materials and properties; 5410 Planetology: Solid Surface Planets: Composition; 5480 Planetology: Solid Surface Planets: Volcanism (8450); *KEYWORDS*: Mars, Mars Global Surveyor, thermal emission spectrometer, MGS, TES

**Citation:** Wyatt, M. B., H. Y. McSween Jr., J. E. Moersch, and P. R. Christensen, Analysis of surface compositions in the Oxia Palus region on Mars from Mars Global Surveyor Thermal Emission Spectrometer Observations, *J. Geophys. Res.*, 108(E9), 5107, doi:10.1029/2002JE001986, 2003.

## 1. Introduction

[2] Atmospherically corrected thermal emissivity data [Bandfield *et al.*, 2000a; Smith *et al.*, 2000] from the Mars Global Surveyor (MGS) Thermal Emission Spectrometer (TES) have been used to identify two unique global-scale surface lithologies [Bandfield *et al.*, 2000b; Christensen *et al.*, 2000a]. Surface type 1 and type 2 spectral units are divided roughly along the planetary dichotomy that separates ancient, heavily cratered crust in the southern hemisphere from younger lowland plains in the north [Bandfield

*et al.*, 2000b; Rogers *et al.*, 2001]. The surface type 1 spectral end-member is characterized by high abundances of plagioclase and pyroxene and is interpreted as largely unweathered basalt [Christensen *et al.*, 2000a; Bandfield *et al.*, 2000b; Hamilton *et al.*, 2001]. The surface type 2 spectral end-member has been interpreted either as andesite with high modal plagioclase and volcanic glass and low modal pyroxene [Bandfield *et al.*, 2000b; Hamilton *et al.*, 2001] or as partly weathered basalt with high modal plagioclase and alteration phases (clays and silica coatings) and low modal pyroxene [Wyatt and McSween, 2002].

[3] The Oxia Palus quadrangle on Mars is unique in that it encompasses the geographic and compositional transition between the southern highlands and northern lowlands and

surface type 1 and 2 lithologies, as well as past spacecraft landing sites that may provide ground truth for spectral interpretations from orbit. In this study, we examine the distribution of TES-derived surface type 1 and 2 materials in Oxia Palus through high-spatial-resolution mapping and integrate Mars Orbiter Camera (MOC) and Mars Orbiter Laser Altimeter (MOLA) data sets for a detailed description of the Martian surface. The diversity of observable landforms in Oxia Palus, which reflect both active geologic processes and remnants of paleoclimate effects, has made this one of the most studied regions on Mars. Features of interest within Oxia Palus for this study include volcanic/sedimentary materials in southern Acidalia Planitia, low-albedo crater floors and wind streaks in western Arabia Terra, and the channel outflow deposits of the Mars Pathfinder (MP) landing site in Chryse Planitia. We also attempt to fit the basalt and andesite/weathered basalt interpretations of the TES surface types into multiple working hypotheses to describe the origin of surface materials on local and regional scales.

## 2. Geologic Setting

[4] Within the Oxia Palus quadrangle ( $0^{\circ}$ – $45^{\circ}$ W longitude,  $0^{\circ}$ – $30^{\circ}$ N latitude), the northern lowland terrains of Chryse and Acidalia Planitiae are bounded by the southern highland terrains of Xanthe and Arabia Terrae (Figure 1, MOC Composite Image). Relative ages of northern lowland materials based on the crater-density stratigraphy of *Tanaka* [1986] range from Late Noachian to Early Amazonian, while older southern highland materials range in age from Middle Noachian to Early Hesperian. In ascending stratigraphic order, the exposed surface units within the Oxia Palus quadrangle are (1) the Middle to Late Noachian southern-cratered terrain, (2) the Hesperian-aged Vastitas Borealis Formation, a unit interpreted to be degraded lava flows and sediments, (3) Hesperian-aged outflow channel deposits at the margins of the lowlands in Chryse Planitia, and (4) various local Amazonian-aged plains units [*Head et al.*, 2002].

### 2.1. Northern Lowlands

[5] Chryse Planitia makes up the southern portion of a basin with elevations ranging from 0 to  $-2000$  m (relative to geoid) and grades north into Acidalia Planitia with elevations decreasing to  $-4000$  m. Several large outflow channels (Ares, Simud, and Tiu Valles) empty into Chryse Planitia and eventually grade into broad relatively smooth plains further north in Acidalia Planitia. The MP landing site was selected in Chryse Planitia partly because of the expected high rock abundances [*Edgett and Christensen*, 1997] in the Ares and Tiu Valles outflow deposits. High rock abundances at the landing site were confirmed by Imager for Mars Pathfinder (IMP) observations that showed the area to be strewn with large boulders, although with significant amounts of surface dust coatings [*McSween et al.*, 1999]. Chryse and Acidalia Planitiae landforms and surface materials have been variously interpreted as subaerially emplaced mass flows [*Tanaka*, 1997], coastal marine [*Parker et al.*, 1993], and residual sedimentary deposits [*Head et al.*, 2002]. A curved dashed white line displayed in Figure 1 marks the extent of a proposed ancient shoreline

for a large standing body of water in southern Acidalia Planitia [*Parker et al.*, 1993; *Head et al.*, 1999]. A curved solid white line in Figure 1 marks the southern extent of the Vastitas Borealis Formation [*Head et al.*, 2002].

### 2.2. Southern Highlands

[6] Xanthe Terra is part of the heavily cratered highlands and is cut by long systems of grabens in the Valles Marineris system of canyons to the west. Arabia Terra has numerous impact craters with large low-albedo wind streaks emanating from low-albedo areas on crater floors. Most models for the formation of dark intracrater materials involve the entrapment of sand-sized particles that can be transported into, but not out of, craters by wind [e.g., *Arvidson*, 1974; *Christensen*, 1983; *Thomas*, 1984]. Several hypotheses exist for the origin of adjacent low-albedo wind streaks. Some models interpret them to be a result of saltation and traction [e.g., *Arvidson*, 1974; *Thomas et al.*, 1981], consisting of sandy material deflated from adjacent dark intracrater deposits; other models interpret them to be the result of material being stripped from the surface revealing a darker substrate [e.g., *Soderblom et al.*, 1978]. More recent models have proposed that streaks form by the deposition of fine dark silt from plumes of suspended material [*Thomas and Veverka*, 1986]. This view is now supported by MOC observations that suggest the dark materials are mantle deposits of fine-grained sediment deflated from adjacent crater floors not sand-sized particles [*Edgett*, 2002].

[7] The Sinus Meridiani and Aram Chaos hematite regions in Terra Meridiani identified by TES also occur partly within the Oxia Palus quadrangle [*Christensen et al.*, 2000b, 2002]. A range of possible mechanisms for the formation of coarse-grained, crystalline hematite on Mars was critically examined by *Christensen et al.* [2000b], with a favored interpretation proposed as in-place sedimentary units composed primarily of basaltic sediment with  $\sim 10$ – $15\%$  crystalline gray hematite.

## 3. Data Sets

### 3.1. Thermal Emission Spectrometer

[8] Thermal infrared spectral observations by the TES instrument cover the wavelength range from  $1655$  to  $200\text{ cm}^{-1}$  ( $\sim 6$  to  $50\text{ }\mu\text{m}$ ) at  $10$  or  $5\text{ cm}^{-1}$  sampling [*Christensen et al.*, 1992]. A complete description of the TES instrument, radiometric calibration, and instrument-related errors is given by *Christensen et al.* [2001]. Spectra used for analysis of surface compositions were collected from the start of the mapping orbit data set up to orbit 5317 (ock 7000,  $L_s$  104–352). The orbit range is restricted because of an anomaly, possibly resulting from vibrations with the MGS spacecraft, that causes a sporadic minor feature to appear in TES spectral data at  $\sim 1000\text{ cm}^{-1}$  in orbits after 5317. Only data at  $10\text{ cm}^{-1}$  sampling are examined in this study, which is approximately 99% of the total data collected from this orbit range. Spectra are limited to those with surface temperatures  $>250\text{K}$ , dust extinctions of  $<0.18$  ( $1075\text{ cm}^{-1}$  opacity of approximately 0.3), and water ice extinctions of  $<0.1$  ( $800\text{ cm}^{-1}$  opacity of approximately 0.15) to ensure a high surface signal to noise ratio [*Bandfield et al.*, 2000a]. A data restriction of emission

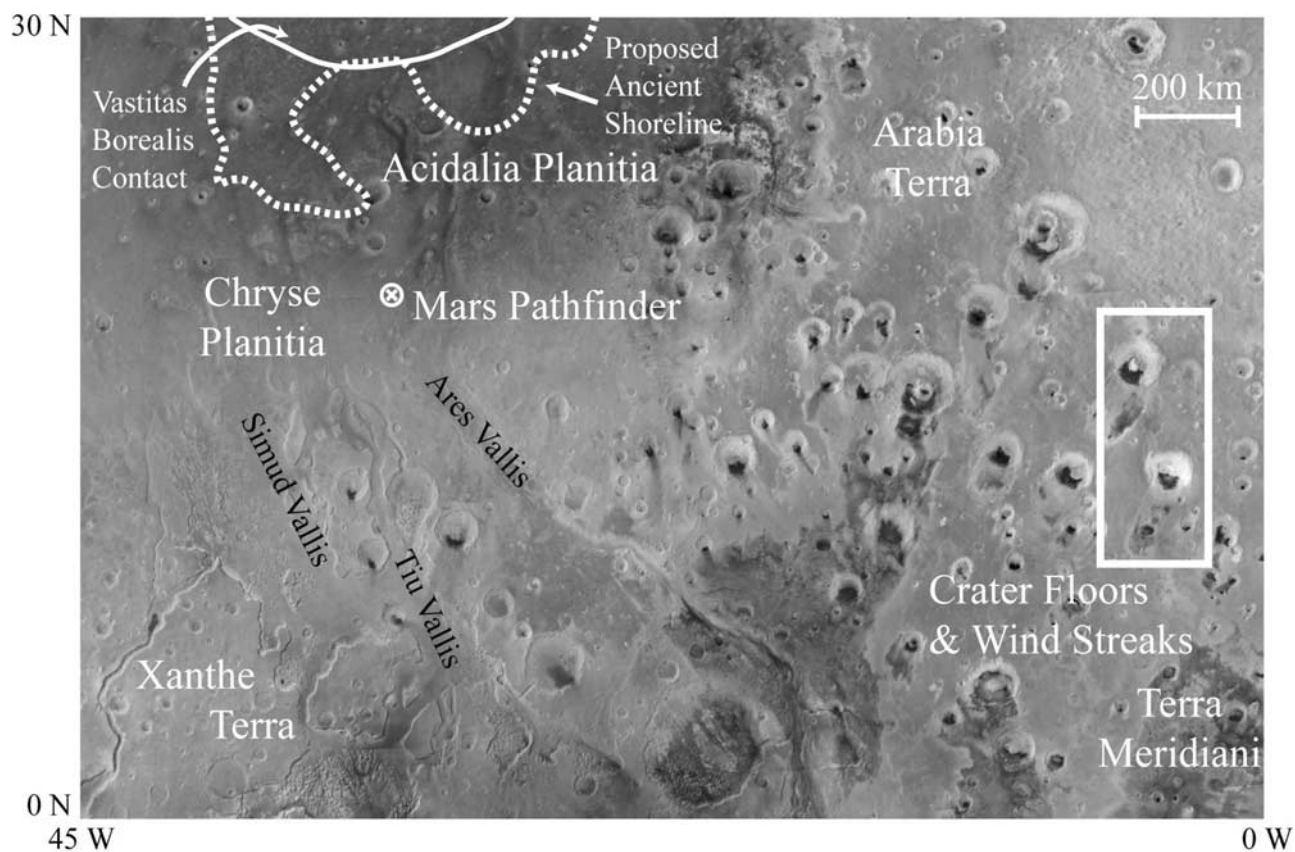


**Figure 1.** Composite MOC images of Oxia Palus quadrangle. Areas of interest include volcanic/sedimentary materials in southern Acidalia Planitia, low-albedo impact crater floors and adjacent wind streaks, and the Mars Pathfinder landing site and Ares and Tiu Valles source regions.

angles  $<30^\circ$  is applied everywhere except the MP landing site, when higher multiple emission angles are examined in an effort to analyze rock surfaces with less bright dust coverings. Multiple emission angle observations, or emission phase functions (EPF), are taken with the TES pointing mirror at several angles in the fore and aft direction during orbit passes creating a mosaic of the targeted surface. Fine-grained dust closely resembles a featureless blackbody spectrum in the wavelengths studied and can mask underlying rock compositions from analysis if sufficient coverings are present [Crisp and Bartholomew, 1992].

[9] TES emissivity spectra are linearly deconvolved using average global Martian surface and atmospheric spectral end-members [Bandfield *et al.*, 2000a, 2000b; Smith *et al.*, 2000] to derive surface compositions in Oxia Palus. The least squares fit algorithm, output results, and method used are fully described by Ramsey and Christensen [1998], Bandfield *et al.* [2000a], Christensen *et al.* [2000a], and Smith *et al.* [2000]. The surface type 1 and 2 [Bandfield *et al.*, 2000b] spectral end-members, mixtures of the two units, and hematite [Christensen *et al.*, 2000b] have been demonstrated to represent accurately the surface composition of all major low-albedo regions on Mars covered by TES [Bandfield *et al.*, 2000b].

[10] Concentrations of surface type 1 and 2 materials, derived from the linear deconvolution of individual TES emissivity spectra, are binned and averaged into maps of 8 and 16 pixels/degree for regional and high-resolution

views, respectively. One square pixel in a TES high-resolution composition map represents approximately a 3.7 km by 3.7 km area at the Martian equator. Each measured TES spectrum represents the average emissivity of an approximate 3 km by 9 km footprint on the Martian surface. Surface concentrations from overlapping TES spectra are averaged within the TES composition maps to improve the signal to noise ratio. The elongated pixel dimension for measured TES spectra is due to the final mapping orbit of MGS being reversed relative to the Martian surface because of a damaged solar panel that caused an extended aerobraking phase. Image motion compensation was originally designed to compensate for the MGS orbit direction; however, it does not produce the intended result when stepping the targeting mirror in a direction opposite that which was originally intended. Averaging derived surface compositions from TES emissivity spectra from different orbits raises the possibility that different atmospheric conditions were present during data collection. However, data are filtered to exclude extreme atmospheric conditions (dust storms, ice clouds), and atmospheric components have been demonstrated by Bandfield *et al.* [2000a] to combine linearly.

[11] To better understand the physical nature of surface materials, we also examine thermal inertia values derived from TES bolometric thermal radiance (5.1 to 150  $\mu\text{m}$ ) measurements. Thermal inertia is the primary factor controlling the amplitude of the diurnal variation of surface

temperature and is most strongly dependent on the thermal conductivity of the surface materials. Thermal inertia is defined as a combination of thermal conductivity  $k$ , density  $\rho$ , and heat capacity  $c$ :

$$I \equiv \sqrt{k\rho c} \quad (1)$$

Thermal inertia depends primarily on the average particle size of the grains comprising the surface, the size and abundance of rocks on and near the surface, and the degree of induration of duricrust. Low-albedo regions make up about 50% of the Martian surface and have thermal inertias and spectral contrasts expected for sand-sized particles [e.g., Kieffer *et al.*, 1977; Presley and Christensen, 1997], enabling detailed analysis of surface compositions. For a complete description of how thermal inertia is calculated, see Mellon *et al.* [2000].

### 3.2. Mars Orbiter Camera

[12] MOC narrow angle (NA) and wide angle (WA) images are obtained at spatial resolutions of 1.5 to 6 m/pixel and 240 to 7500 m/pixel respectively. A description of the MOC instrument is detailed by Malin and Edgett [2001]. Available images for this study were acquired between September 1997 and December 2001, and all images were obtained with the MGS spacecraft in a nadir-viewing orientation. WA mosaics are provided courtesy of NASA/JPL/Malin Space Science Systems and provide the context for NA images that are used for high-resolution detailed mapping.

### 3.3. Mars Orbiter Laser Altimeter

[13] MOLA topography data are used to create digital topographic maps and 3-D shaded relief images of the Martian surface in Oxia Palus. For a complete description of the MOLA instrument, analytical techniques, and instrument-related errors, see Zuber *et al.* [1992]. MOLA data are binned in a  $\sim 500$  m/pixel grid and are used as a base map for overlaying TES compositional maps and MOC NA and WA images.

### 3.4. Data Set Registration

[14] The TES, MOC, and MOLA data sets are all defined by latitude and longitude coordinates. When these data sets are translated to a map projection, each data set will also be defined in a Cartesian coordinate system as described by the selected projection. Map projected TES compositional images, MOC composite images, and MOLA digital elevation maps (DEMs) are aligned in ArcView (ESRI) based on their Cartesian coordinates. In ArcView, for raster data sets, this is expressed by the top left pixel location and the pixel dimension in map units (i.e., meters). Each data set can then be overlain and merged together within the ArcView software interface. Changes to map locations can also be done manually to compensate for any small offsets in registration of map-projected images.

## 4. Distribution of TES Surface Compositions

### 4.1. Regional View

[15] Figure 2 shows the regional distribution of surface type 1 (green) and 2 (red) lithologies in Oxia Palus derived from linear deconvolution of TES emissivity spectra. Blue

pixels on the TES composition map represent areas covered by fine-grained bright dust, which sufficiently blankets the surface to prohibit spectral analysis of sand and rock compositions (particle diameters of 10  $\mu\text{m}$  or less and a mantle thickness of tens of microns) [e.g., Ruff and Christensen, 2002]. The “concentration” of fine dust was determined not from linear deconvolution but instead by using the derived TES data set index parameter “long-wavelength depth,” which distinguishes between bright and dark regions. This parameter has proven useful in mapping where coarse particles are located on the Martian surface, and hence where fine dust is absent, and correlates very well with albedo and thermal inertia [Bandfield, 2000]. Yellow pixels indicate mixing of surface type 1 and 2 materials, whereas black stripes and pixels indicate lack of TES surface coverage.

[16] Surface type 1 dominates the southern highlands of Xanthe Terra and southern Arabia Terra, and surface type 2 dominates northern Acidalia Planitia. Both surface types coincide well with observed low-albedo regions, despite the higher uncertainty with surface type 2 because of random and systematic noise inherent in this spectral signature [Bandfield *et al.*, 2000a]. A mixing/transition from surface type 1 to surface type 2 (south to north) compositions is observed in low-albedo regions marking the southern extent of Acidalia Planitia and northeastern extent of Chryse Planitia.

[17] The MP Landing site (marked with an X in Figure 2) is located in an area that appears to be near the surface type 1 and type 2 transition in southern Acidalia Planitia. It is difficult to discern if TES observations at this regional scale agree with Mars Pathfinder IMP observations of the landing site showing that the tops of rocks, and surfaces in between rocks, are largely covered by fine-grained dust [McSween *et al.*, 1999]. Ares and Tiu Valles show a similar covering of fine-grained dust. Low-albedo crater floors and wind streaks in western Arabia Terra, however, show strong concentrations of surface type 1 and 2 materials even at a regional scale (outline of box in Figure 2).

### 4.2. Southern Acidalia Planitia

[18] The mixing/transition from surface type 1 to surface type 2 (south to north) compositions in the low-albedo regions of southern Acidalia Planitia is illustrated in Figure 3. Two gray scale TES maps (16 pixels/degree) show the concentrations of surface type 1 and type 2 materials in Figures 3a and 3b, respectively. Figure 3c is a gray scale MOLA shaded relief image sampled at 500 m/pixel, and Figure 3d is a mosaic of MOC images of the same area. Superimposed on all panel images is a curved dashed line marking the extent of a proposed ancient shoreline for a large standing body of water in southern Acidalia Planitia [Parker *et al.*, 1993; Head *et al.*, 1999] and a curved solid line marking the southern extent of the Vastitas Borealis formation [Head *et al.*, 2002]. The images in Figure 3 extend north of 30°N, which marks the northern extent of the Oxia Palus quadrangle, to show the distribution of surface materials in a greater area of Acidalia Planitia. Red boxes indicate locations of TES surface spectra shown in Figure 4.

[19] Figure 3a clearly shows the extent of surface type 1 materials in southern Acidalia Planitia, while Figure 3b

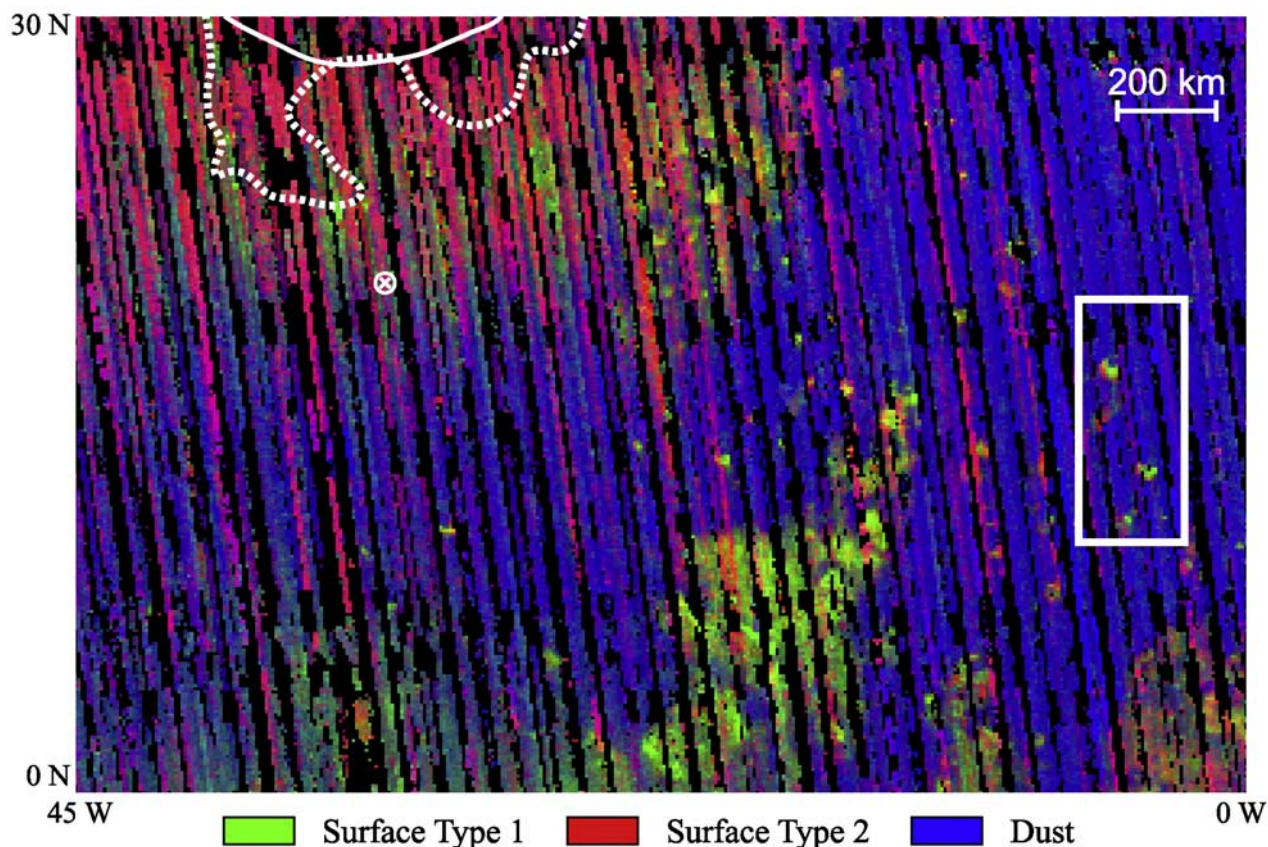


**Figure 2.** TES compositional map of the Oxia Palus quadrangle binned at 8 pixels/degree. Surface type 1 (green) dominates the southern highlands, whereas surface type 2 (red) dominates the northern lowlands. Blue pixels represent areas covered by fine-grained dust.

shows the range of surface type 2 materials across nearly all of Acidalia Planitia. Surface type 1 materials are located predominately south of the proposed shoreline and the Vastitas Borealis formation, while surface type 2 materials dominate to the north and cross over the shoreline. A comparison between Figures 3a and 3b with the MOLA map in Figure 3c shows that surface type 1 materials in the mixing/transition zone occur mainly near the highlands/lowlands transition, whereas surface type 2 materials are concentrated in the northern lowlands of Acidalia Planitia.

[20] Figure 4 compares average TES surface spectra for materials at the southern extent of the mixing/transition band with materials to the north (boxes in Figure 3). Also shown in Figure 4 are the surface type 1 and 2 spectral end-members from *Bandfield et al.* [2000b], offset by 0.02 emissivity for comparison purposes. Within the southern portion of the mixing band, surface components contain a broad, flat absorption between  $\sim 800$  and  $1000\text{ cm}^{-1}$  and absorption through  $\sim 200\text{--}500\text{ cm}^{-1}$ . In the northern transition surface components contain a more V-shaped absorption between  $\sim 800$  and  $1000\text{ cm}^{-1}$  and more uniform slope between  $\sim 200$  and  $500\text{ cm}^{-1}$ . Linear deconvolution of these spectra using the surface type 1 and 2 end-members reveals the surface spectrum from the southern portion of the band is dominated by a surface type 1 component ( $\sim 60$  vol %), but with a significant contribution of surface type 2 material ( $\sim 40$  vol %). The reverse is seen to the north, where the surface spectrum is dominated by a surface

type 2 component ( $\sim 66$  vol %) with a significant contribution of surface type 1 material ( $\sim 34$  vol %).

#### 4.3. Low-Albedo Crater Floors and Wind Streaks

[21] Deconvolved TES spectra of low-albedo intracrater materials in western Arabia Terra reveal both surface type 1 and 2 compositions within individual craters where complete TES coverage is available. Surface type 1 compositions form a central core in dark features on crater floors, whereas surface type 2 compositions form a surrounding arc on the dark downwind sides of crater walls. The transition between these compositions appears to occur at or near the floor-wall interface within some impact craters. Surface type 1 and 2 compositions are also observed in the adjacent low albedo wind streaks; however, a mixing trend is not as evident as within the impact craters. There does not appear to be a discernable compositional difference across (east-west) dark wind streak material and the often observed bright red deposits along their margins.

[22] Figure 5 shows a composite MOC image (Figure 5a), a TES compositional map (Figure 5b), and a TES thermal inertia map (Figure 5c) of Radau and Marth craters, which are outlined by a white box in the MOC composite image of Figure 1 and TES regional view of Figure 2. Radau Crater ( $17.1^\circ\text{N}$ ,  $4.8^\circ\text{W}$ , 114.5 km diameter) and Marth Crater ( $13.0^\circ\text{N}$ ,  $3.5^\circ\text{W}$ , 98.4 km diameter) are representative of many large impact craters in western Arabia Terra that have both an intracrater low-albedo feature on part of the southern

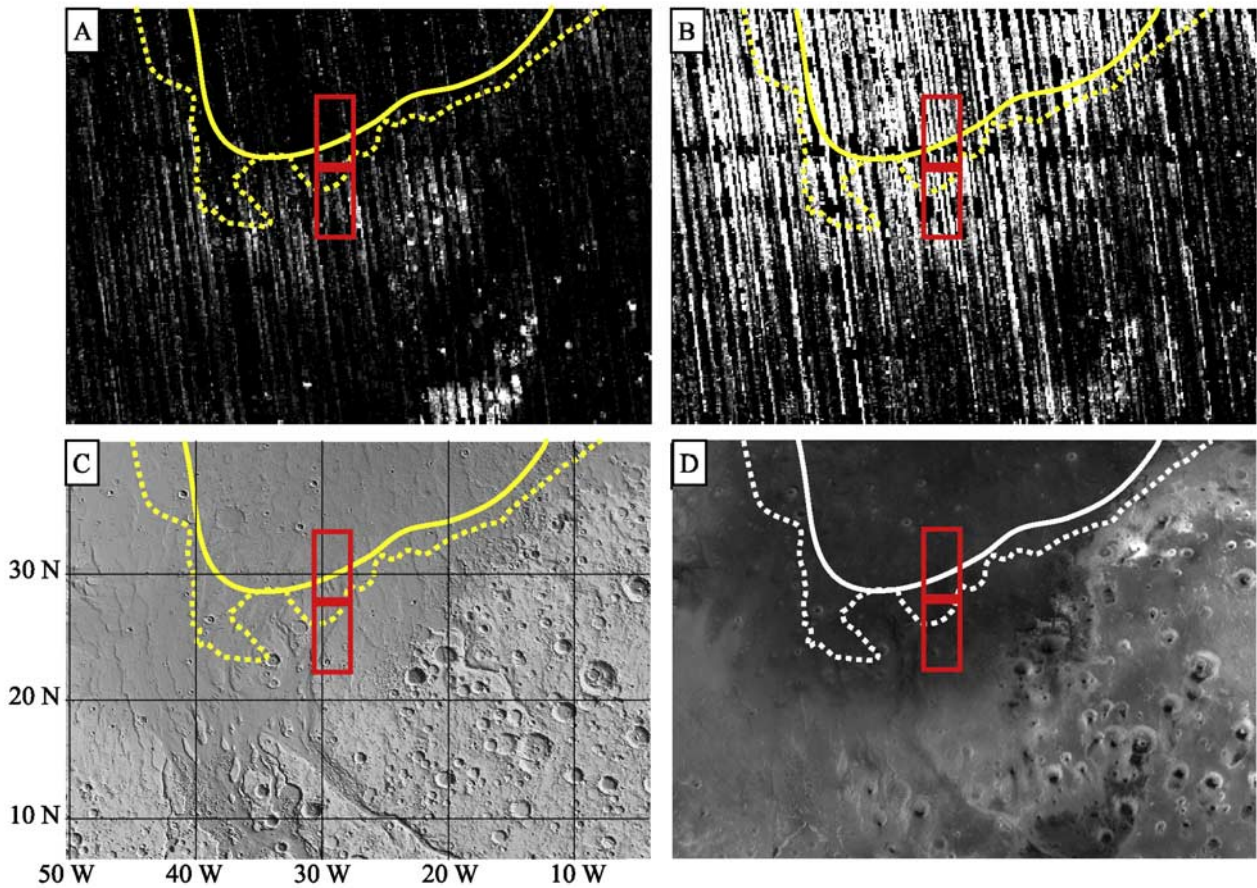


**Figure 3.** (a and b) TES compositional maps, (c) MOLA shaded relief, and (d) MOC composite image of the surface type 1 and type 2 transition in southern Acidalia Planitia. Surface type 1 (bright pixels in Figure 3a) dominates the southern extent of Acidalia Planitia, while surface type 2 (bright pixels in Figure 3b) extends across nearly all of Acidalia Planitia. MOLA topography shows the transition occurs near the northern lowlands-southern highlands boundary. Red boxes indicate locations of spectra shown in Figure 4.

crater floor and an adjacent dark wind streak that extends southward from the dark material (Figure 1). The Radau Crater composition image (Figure 5b) clearly shows the core of surface type 1 (green) and surrounding arc of surface type 2 (red) in the intracater low-albedo feature. The Marth Crater composition image shows the surface type 1 core and part of the surface type 2 rim; however, some dark rim material is not covered by TES observations. The thermal inertia map of Marth Crater (Figure 5c) shows higher values for surface type 1 materials ( $\sim 400\text{--}550 \text{ J/m}^2 \text{ Ks}^{1/2}$ ) compared to surface type 2 materials ( $\sim 300\text{--}400 \text{ J/m}^2 \text{ Ks}^{1/2}$ ). The thermal inertia map of Radau Crater (Figure 5c) partly shows an edge of high thermal inertia material in the low-albedo crater floor, but TES coverage is incomplete. Higher thermal inertias may be interpreted as representing a coarser particle size compared to lower thermal inertias if materials are unconsolidated sediments.

[23] Figure 6 shows a composite MOC image of Radau Crater (southward looking) with superimposed TES composition pixels draped over MOLA topography. The core of surface type 1 and arc of surface type 2 materials on the crater floor and walls are clearly observed. Also shown in Figure 6 is a NA MOC image across the crater floor/wall

interface with a schematic cross section of MOLA topography. The location of the NA MOC image on the MOC composite image is shown in the Radau Crater inset. The transition from surface type 1 to surface type 2 compositions occurs near the crater floor/wall interface and is correlated with a transition from low-albedo dune materials to low-moderate albedo dune-free materials. The absence of dunes in wall materials, and lower measured thermal inertias, may be interpreted as representing finer particle sizes compared to the higher thermal inertia dune material on crater floors.

[24] Figure 7 shows average TES surface spectra for materials within the low-albedo Radau impact crater floor and the slope of crater walls compared to surface type 1 and 2 spectral end-members from *Bandfield et al.* [2000b], which are offset by 0.02 emissivity. Within the impact crater floors, surface components contain a broad, flat absorption between  $\sim 800$  and  $1000 \text{ cm}^{-1}$  and absorption through  $\sim 200\text{--}500 \text{ cm}^{-1}$ , very similar to the surface type 1 end-member. Along the impact crater walls, the surface components contain a V-shaped absorption between  $\sim 800$  and  $1000 \text{ cm}^{-1}$ , similar to the surface type 2 end-member. Linear deconvolution of crater floor and wall spectra using

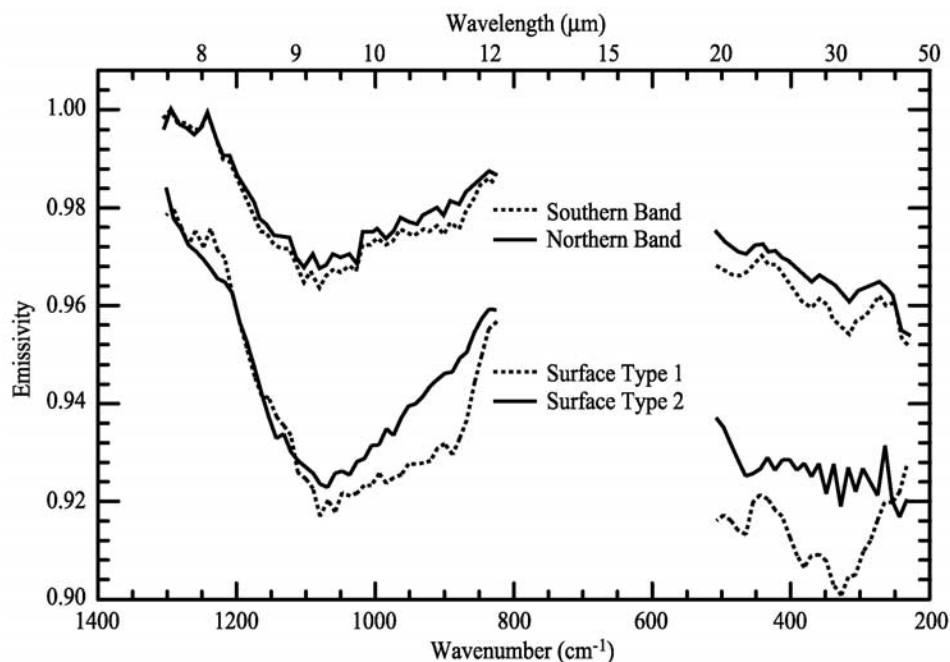


**Figure 4.** Average atmospherically corrected thermal emissivity spectra of the northern and southern transition bands in Acidalia Planitia compared to surface type 1 and type 2 spectral end-members. The southern band is dominated by surface type 1 components ( $\sim 60$  vol %), whereas the northern band is dominated by surface type 2 components ( $\sim 66$  vol %).

the surface type 1 and 2 end-members confirms the general comparison of spectral features. Impact crater floor materials are almost entirely dominated by a surface type 1 component ( $\sim 75$ – $100$  vol %), whereas impact crater wall materials are dominated by surface type 2 material ( $\sim 75$ – $100$  vol %).

#### 4.4. Mars Pathfinder Landing Site and Source Regions

[25] The MP landing site is among the rockiest locations on the planet; however, nearly all of the rocks have significant amounts of surface dust mantles [Smith *et al.*, 1997; McSween *et al.*, 1999]. For this reason, MP offers an ideal opportunity to test whether rock compositions can be resolved in dust-covered regions. Furthermore, the Alpha Proton X-Ray Spectrometer (APXS) analyses of rocks having andesitic compositions [Rieder *et al.*, 1997; McSween *et al.*, 1999] offers ground truth data for interpreting mineralogies and chemistries derived from thermal infrared spectra measured from orbit.

[26] Figure 8 shows a composite MOC image of Chryse Planitia with the MP landing site and arrows indicating flow directions in the Ares and Tiu Valles outflow channels [Tanaka, 1997]. The image is not centered on the MP landing site because the goal of this analysis is to determine whether compositional information can be obtained from both the landing site and its source region to the south. Superimposed on the composite MOC image are boxes representing averaged and binned TES composition pixels at 3.7 km by 3.7 km. At a high-resolution scale, TES coverage of the Martian surface in this region is not complete with data that pass the data filters used in this study. Figure 9a shows a high-resolution MOC NA image of the landing site, with a higher resolution part of the WA mosaic from Figure 8 for reference, and Figure 9b shows an

average TES surface spectrum of the MP landing site compared to the surface type 1 and 2 spectral end-members, which are offset by 0.02 emissivity. Also shown in Figure 9b are average spectra of the Ares and Tiu Valles source regions.

[27] The landing site and source region spectra show much shallower spectral absorptions compared to the surface type 1 and 2 spectra. While there are some spectral absorption features observed in the landing site and source regions spectra, their depths are too small to have confidence in any linear deconvolution results. The tops of rocks and intervening ground surfaces at the landing site were observed to be covered by bright fine-grained dust. The apparent spectral roll-off feature at  $\sim 1150$   $\text{cm}^{-1}$  observed in the MP spectra in Figure 9b is a typical result of fine particle size effects [Christensen *et al.*, 2000a]. The fine-grained surface dust, which closely resembles a featureless blackbody spectrum, thus appears to be sufficiently abundant to obscure analysis of rock compositions from TES observations.

[28] The TES instrument is capable of making emission phase function (EPF) observations by using a pointing mirror to measure a surface at various emission angles along an orbital track. Such measurements could potentially enable TES to observe the sides of rocks at the Mars Pathfinder landing site, instead of only the top surfaces which are covered by fine-grained dust. The sides of rocks at the landing site were commonly observed by the IMP camera to have lower albedos compared to the tops of rocks [Smith *et al.*, 1997] and were targeted by the APXS instrument for chemical analyses of dust-free surfaces.

[29] Figure 10 is a plot of albedo versus Incremental Counter Keeper (ICK) for an EPF mosaic of the MP landing site. ICK is the sequential numbering scheme for observa-

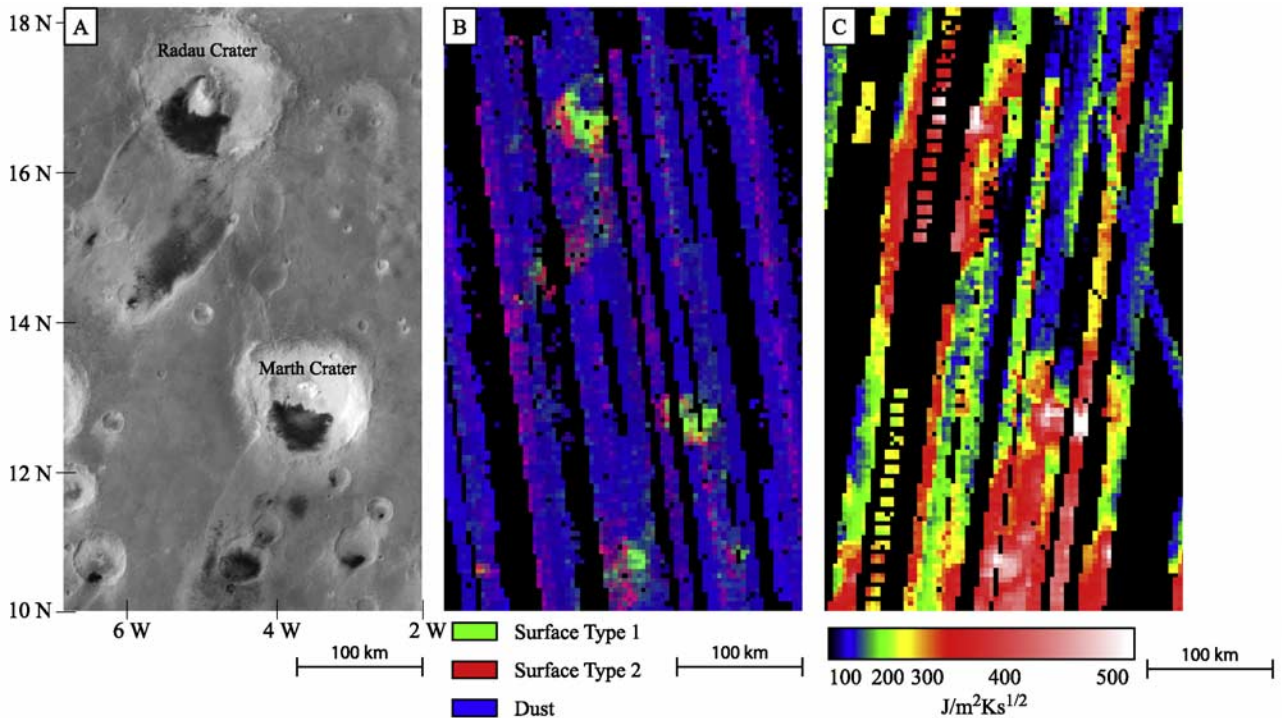


**Figure 5.** (a) Composite MOC image and (b) TES compositional and (c) thermal inertia maps of Radau and Marth impact craters. Low-albedo intracratere materials display a core of surface type 1 material that grades into surface type 2 material along impact crater walls. A similar, but less distinct, trend is observed in low-albedo wind streaks in the downwind direction. Surface type 1 materials generally have higher thermal inertias compared with surface type 2 materials, interpreted as reflecting a coarser particle size.

tions of the TES interferometer and the counter begins at zero at the nightside equator crossing. With increasing ICK, the five data clusters in Figure 10 correspond to different emission angle measurements from forward facing emission observations of  $46^\circ$  and  $26^\circ$ , to one nadir

observation, followed by reverse facing emission angle observations of  $26^\circ$  and  $46^\circ$ . Figure 10 shows that EPF observations at higher emission angles do not result in a significant decrease in surface albedo (note vertical scale), i.e., a greater spectral contribution by nonmantled

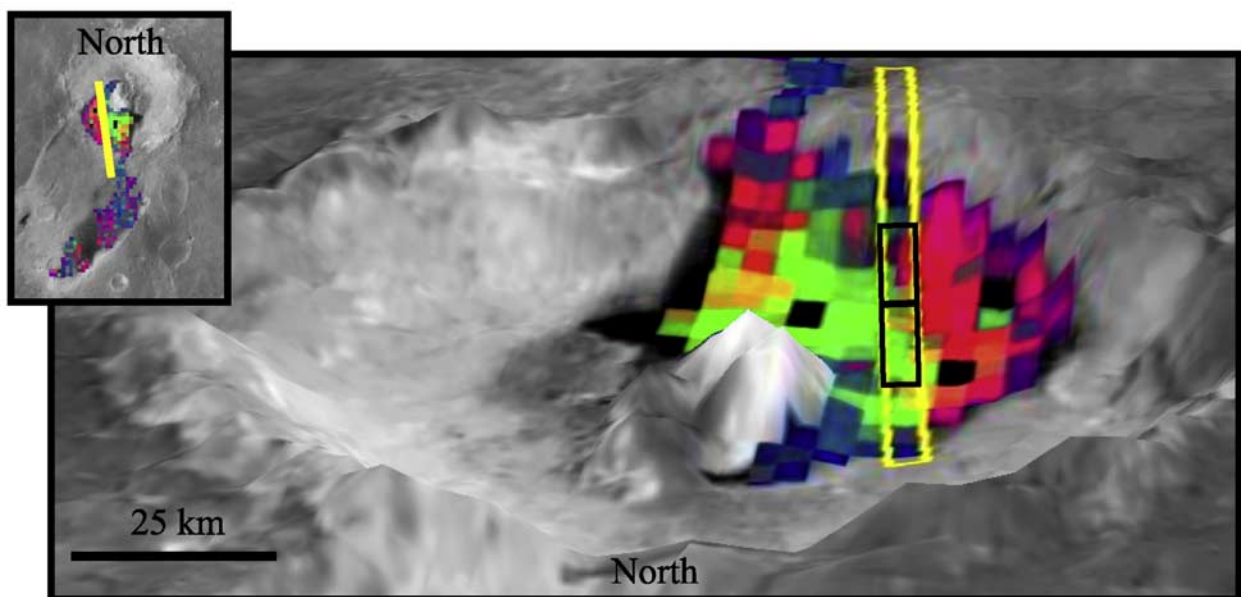


**Figure 6a.** Composite MOC image of Radau Crater (southward looking) with superimposed TES composition pixels draped over MOLA topography.

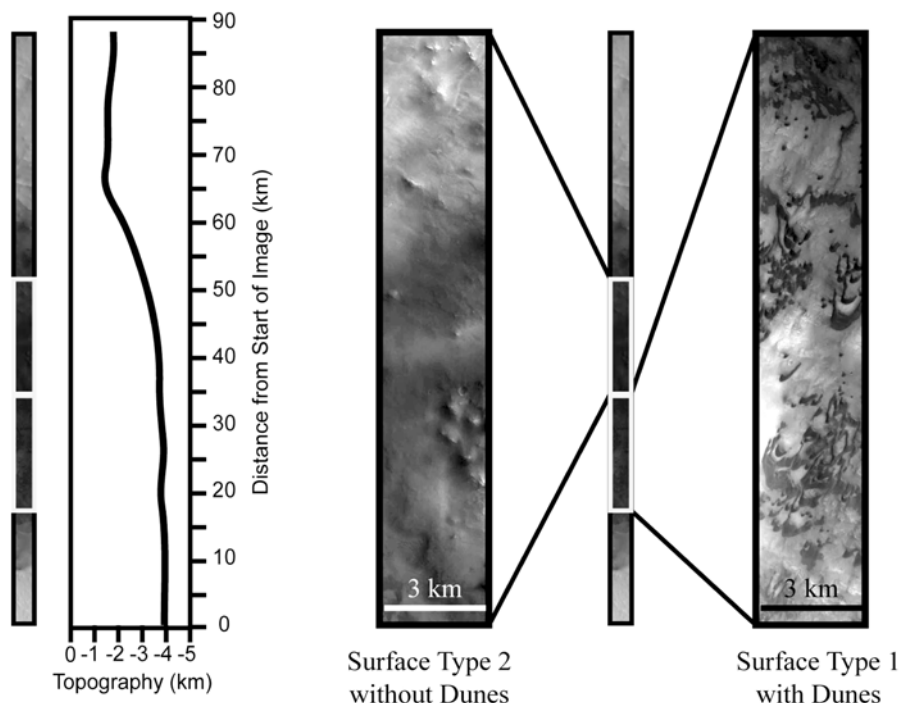


**Figure 6b.** NA MOC images across the crater floor/wall interface with a schematic cross section of MOLA topography. The transition from surface type 1 to surface type 2 compositions occurs near the crater floor/wall interface and is correlated with a transition from low-albedo dune materials to low-moderate albedo dune-free materials.

rock surfaces. This is possibly due to the increased amount of atmospheric dust observed with increasing emission angle observations through longer Martian atmosphere pathlengths. The composition of atmospheric and surface dust is still very uncertain, which makes their removal from EPF observations difficult. For this reason, EPF observations of the MP landing site cannot be used to analyze sides of rocks at this time.

## 5. Discussion

[30] The distributions of surface type 1 and 2 materials, combined with the basalt [Christensen *et al.*, 2000a; Bandfield *et al.*, 2000b; Hamilton *et al.*, 2001] and andesite [Bandfield *et al.*, 2000b; Hamilton *et al.*, 2001] or weathered basalt interpretations [Wyatt and McSween, 2002], allow for multiple working hypotheses to describe the origins of these materials. In the following sections we reinterpret the mixing/transition of surface type 1 and 2 materials in southern Acidalia Planitia and low-albedo impact crater floors and adjacent wind streaks in western Arabia Terra and attempt to fit TES observations to models describing the sedimentary and igneous history of Oxia Palus.

### 5.1. Southern Acidalia Planitia

[31] In the following discussion, we examine three geologic models involving transport of material and/or in-place aqueous alteration to describe the observed transition from surface type 1 to type 2 materials in southern Acidalia Planitia. The transport models are “dry” or “wet” and require the movement of material

from the southern highlands to northern lowlands via large outflow channels in Chryse Planitia. The “dry” transport model is analogous to the subaerially emplaced mass flow model proposed by Tanaka [1997] that does not involve or require water as a means for mass movement. The “wet” transport model is analogous to the residual sedimentary deposit model proposed by Head *et al.* [2002] that involves the deposition of water and sedimentary material in the northern basin and the subsequent loss of water and formation of a residual sedimentary layer. The third geologic model is an indigenous aqueous-alteration hypothesis, analogous to a coastal marine model proposed by Parker *et al.* [1993] that involves the alteration of in-place volcanic materials beneath an ancient northern ocean. Figure 11 refers to all three geologic models that are described in detail in the following sections.

#### 5.1.1. Mixture of Basalt and Andesite

[32] Subaerially emplaced “dry” mass flows [Tanaka, 1997] could explain the observed mixing band of surface type 1 and type 2 compositions if interpreted as basalt and andesite. Surface type 1 material transported to southern Acidalia Planitia by large outflow channels in Chryse Planitia originated toward the southern highlands, which is dominated by basaltic materials (Figure 11). The basalt-dominated mixing band marking the southern extent of Acidalia Planitia could represent the maximum extent of sediment transport from these channels. In this scenario, the andesite in central Acidalia is interpreted as regionally indigenous volcanic material that was partly covered and mixed with basaltic sand transported from the south (Figure 11). Transported basaltic materials would thus also

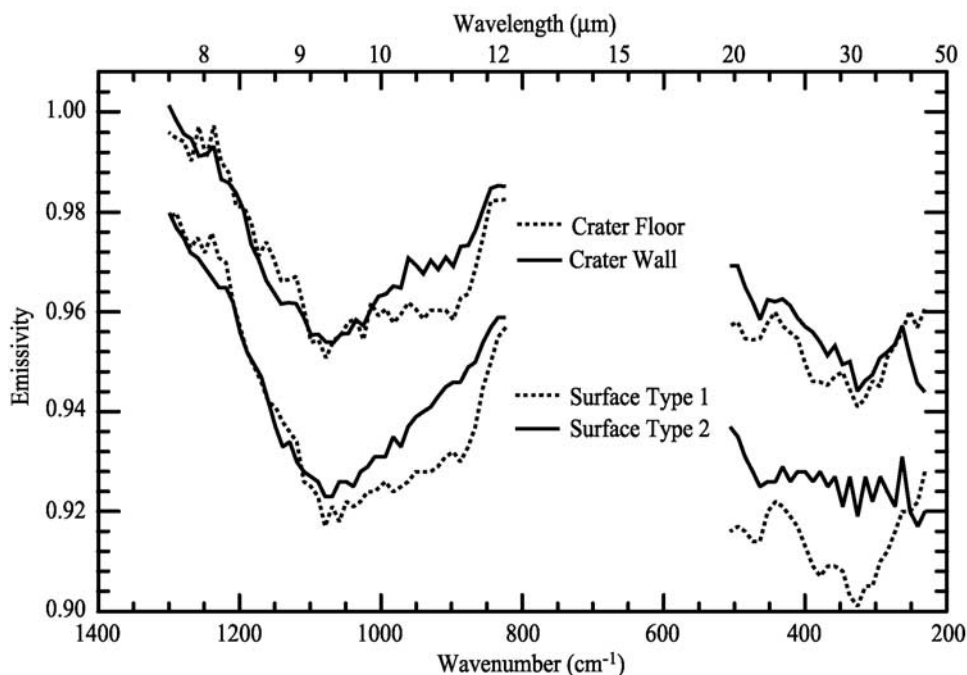


**Figure 7.** Average atmospherically corrected thermal emissivity spectra of low-albedo intracater materials compared to surface type 1 and type 2 spectral end-members. The crater floor is dominated by surface type 1 components, whereas the crater wall is dominated by surface type 2 components.

dominate beneath the dust-covered region between this band and the basalt-dominated southern highlands.

#### 5.1.2. Mixture of Basalt and Weathered Basalt

[33] Residual sedimentary “wet” deposits [Head *et al.*, 2002] and/or indigenous coastal marine sediments [Parker *et al.*, 1993] could explain the observed mixing band of surface type 1 and 2 compositions if interpreted as basalt and weathered basalt. Figure 11 shows the extent of the Hesperian Vastitas Borealis Formation in southern Acidalia Planitia, which has been interpreted as a thin veneer of residual sediment deposited on top of older Hesperian ridged material [Head *et al.*, 2002]. The Vastitas Borealis formation occupies about 45% of the entire northern lowlands [Tanaka and Scott, 1987] and has been proposed by Head *et al.* [2002] to represent material transported to the north by large volumes of water. Also shown in Figure 11 are geomorphic contacts previously interpreted as ancient shorelines [Parker *et al.*, 1993]. The elevations of these contacts have been examined with high-resolution MOLA data and found to approximate an equipotential line [Head *et al.*, 1999], supporting the hypothesis of an ancient ocean basin.

[34] In a “wet” deposit model, surface type 1 material originating in the basalt-dominated southern highlands was transported to southern Acidalia Planitia by floods that carved the large outflow channels in Chryse Planitia. The transported basaltic material was altered where water ponded and was later deposited as a thin residual veneer (Vastitas Borealis Formation) when the water was lost. Figure 11 shows that the Vastitas Borealis formation contact coincides very well with the transition between surface type 1 basalt and type 2 weathered basalt.

[35] In an indigenous coastal marine model, the transition between the two surface types marks the southern

extent of submarine alteration of indigenous basalt caused by large bodies of standing water in the northern lowlands. Proposed shoreline contacts in Chryse and Acidalia Planitiae (Figure 11) also coincide very well with the transition zone between surface type 1 basalt and type 2 weathered basalt. The basalt-dominated band and large volume of weathered basalt in central Acidalia are both interpreted in this scenario as indigenous materials reflecting a progression of more advanced alteration of basalt toward deeper water levels.

[36] The wet transport model does not directly address the presence or absence of long-term, large standing bodies of water (oceans?) in the northern lowlands. It does, however, provide possible insight into the origin of some unusual surface properties in the region. The northern lowlands, including southern Acidalia Planitia, are extremely smooth at several scale lengths, comparable to abyssal plains on Earth [e.g., Smith *et al.*, 1998; Aharonson *et al.*, 1998; Head *et al.*, 2002]. The emplacement of aqueously altered outflow channel deposits could provide a mode of formation for this smoothing [Head *et al.*, 2002]. This explanation does not preclude the presence of oceans, as they could have existed prior to material transport (Noachian [e.g., Clifford and Parker, 2001]). However, in this case, sediment transported into preexisting large bodies of water and later deposited would result in a similar thin veneer of altered material (Vastitas Borealis formation).

[37] In summary, the basalt and andesite/weathered basalt interpretations allow for multiple working hypotheses to describe the origin of the surface type 1 and type 2 mixing/transition in southern Acidalia Planitia. The “dry” transport model and “wet” transport and/or indigenous coastal marine models fit within existing geologic scenarios describing the sedimentary and volcanic history of the region.

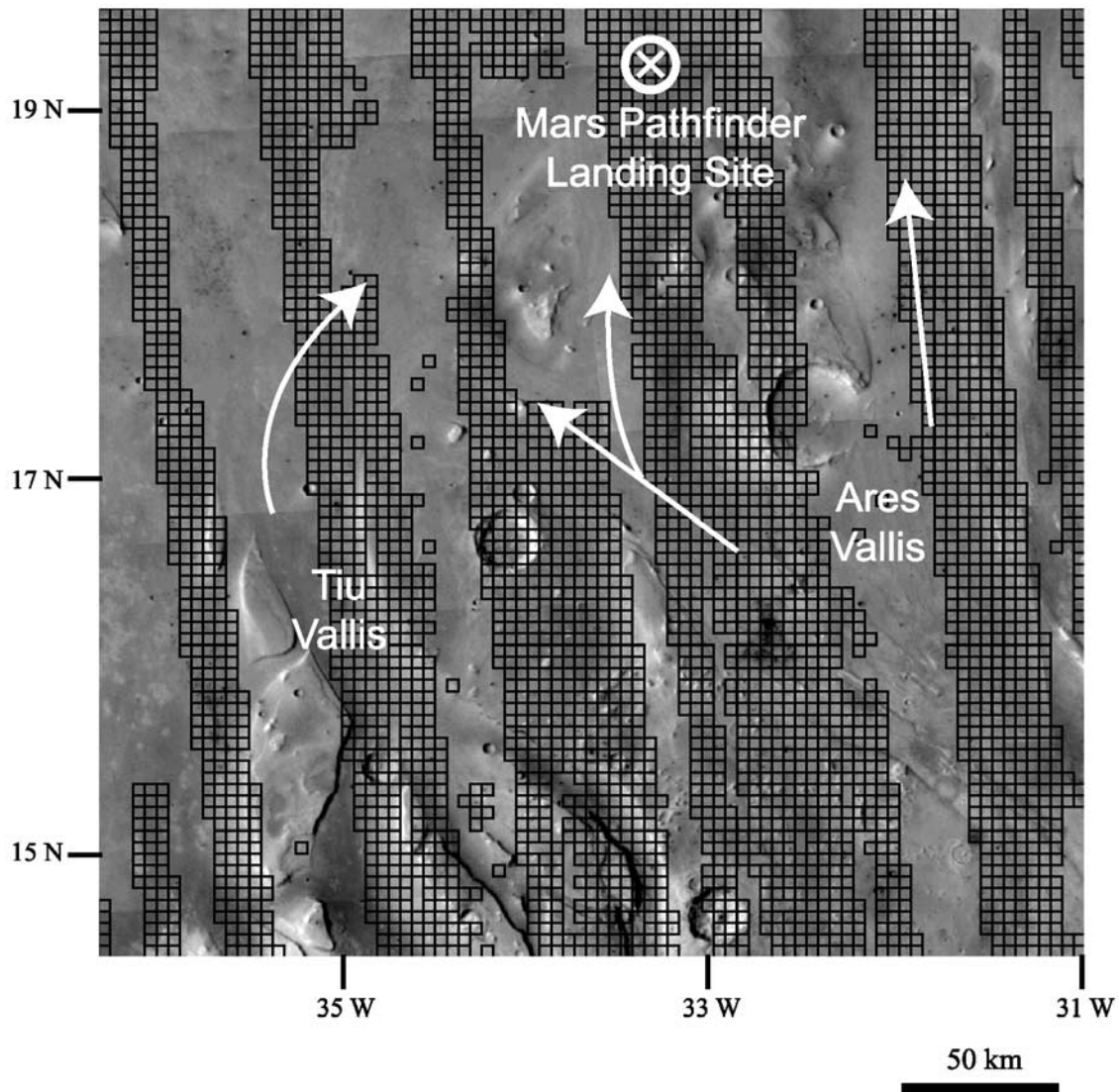


**Figure 8.** TES 16 pixels/degree compositional coverage superimposed on a composite MOC image of Chryse Planitia with the Mars Pathfinder landing site and Ares and Tiu Valles source regions.

## 5.2. Low-Albedo Intracrater Materials and Wind Streaks

[38] The physical properties of, and genetic link between, low-albedo intracrater materials and wind streaks in Oxia Palus and western Arabia Terra have been the subject of considerable study and debate for three decades [e.g., Sagan *et al.*, 1972; Arvidson, 1974; Peterfreund, 1981; Christensen, 1983; Thomas, 1984; Edgett and Christensen, 1994; Edgett and Malin, 2000]. Most models describing the origin and formation of these features are based on visible observations and thermal inertia measurements. We attempt to fit the TES compositional interpretations of basalt and andesite/weathered basalt for surface type 1 and type 2 materials into various origin hypotheses to provide insight into formational processes.

### 5.2.1. Low-Albedo Intracrater Materials

[39] Models for the formation of dark intracrater floor material generally involve the entrapment of sand-sized

particles that can be transported into, but not out of, craters by wind [e.g., Arvidson, 1974; Christensen, 1983; Thomas, 1984]. These features correlate with surface type 1 basaltic compositions identified in the low-albedo floors of impact craters (Figure 6). Supporting evidence for an eolian origin of these materials comes from Mariner 9, Viking, and MOC high-resolution observations of barchan dune fields [e.g., Sagan *et al.*, 1972; Arvidson, 1974; Peterfreund, 1981; Christensen, 1983; Thomas, 1984; Edgett and Christensen, 1994; Edgett and Malin, 2000]. Observations of a consistent orientation in a downwind direction for many dark intracrater features and high thermal inertia values further support the hypothesis that these materials are eolian in origin, sand-sized, and marginally mobile.

[40] High-resolution MOC images have shown that dunes are not observed in low-albedo material covering the southern walls and rims of the same impact craters. This material correlates with surface type 2 compositions

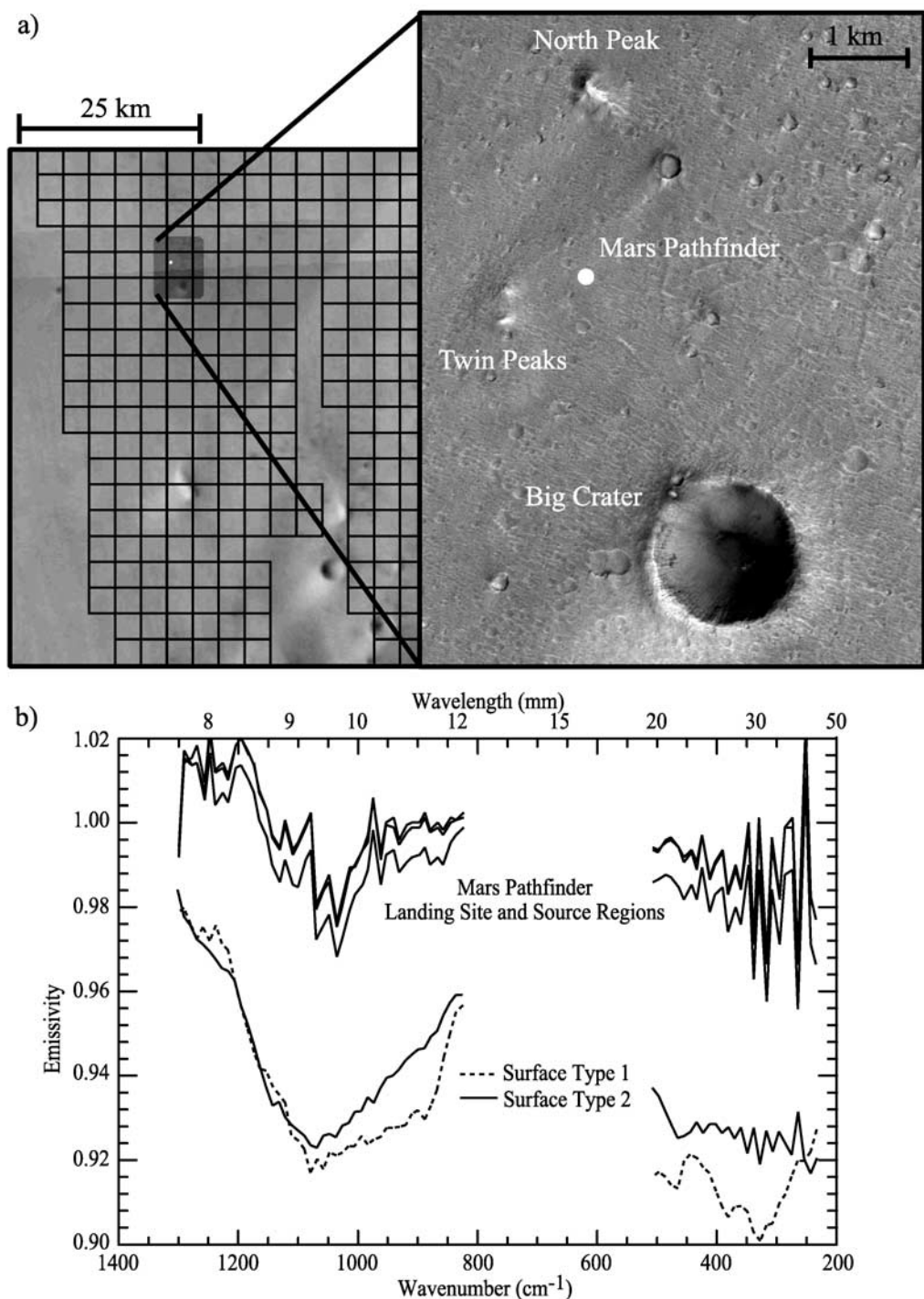


**Figure 9.** (a) High-resolution NA MOC image of the Mars Pathfinder landing site with (b) thermal emissivity spectra of the landing site and source regions compared to surface type 1 and type 2 spectral end-members. Landing site and source region spectra display very shallow absorptions compared to surface end-members as a result of fine-grained dust cover.

that form an arc around intracrater surface type 1 basaltic floor materials. Sorting of particle sizes blown into craters and up onto crater walls could be controlling the observed spatial distribution of surface type 1 and type 2 materials. The thermal inertia map in Figure 5 clearly shows a decrease in thermal inertia, interpreted as indicating a

fining of material, from the center of low-albedo crater floors south to crater walls in Radau and Marth craters. If this is true, fine material on crater walls has to be coarser than dust.

[41] Differences in particle sizes between crater floors and walls could possibly reflect differences in the mineralogies

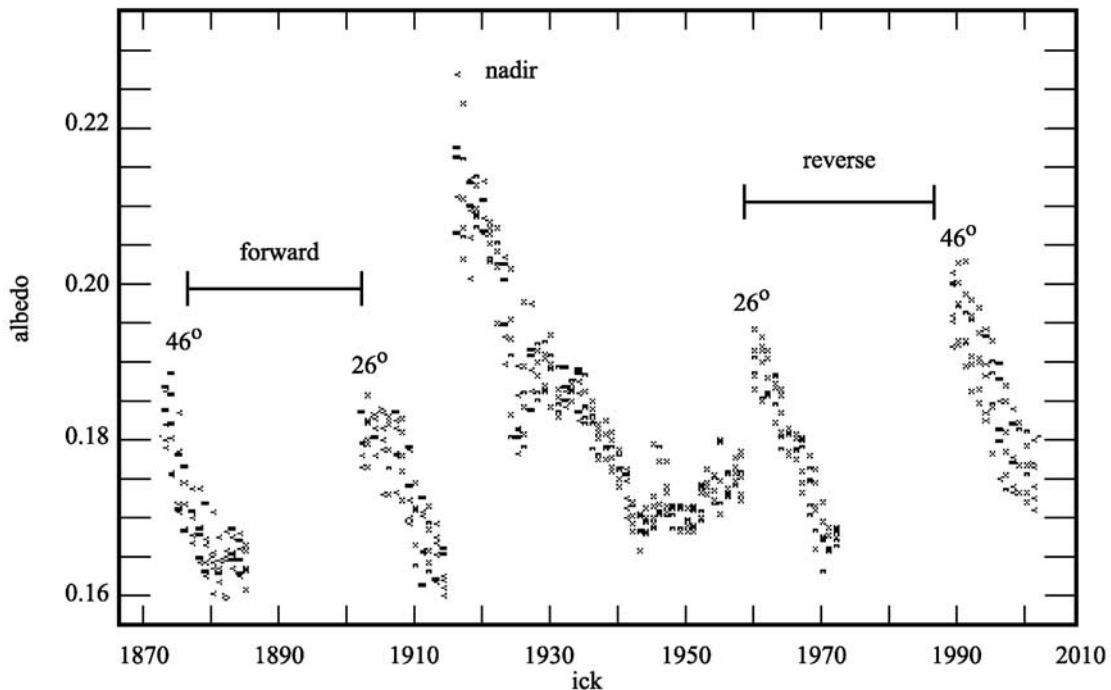


**Figure 10.** Plot of albedo versus Incremental Counter Keeper (ICK) for an EPF mosaic of the MP landing site. EPF observations at higher emission angles do not result in a significant decrease in surface albedo, i.e., increase in rock observations, at the landing site. This is due to the increased amount of atmospheric dust observed with increasing emission angle observations.

of the respective surfaces. The coarsest basalt material near the center of the crater floor may grade to finer surface type 2 material transported further downwind (southward) and partially up crater walls. The deconvolved andesite and weathered basalt mineralogies for surface type 2 contain significantly more glass and/or clay compared to surface type 1 basaltic materials. In a physical weathering environment, such as the eolian regime that transported material along the floors and up onto the walls of craters, lithologies containing glass and/or clay (surface type 2) will break down into smaller particles compared to lithologies with less modal abundances of these components (surface type 1). The mineralogies of the two surface types blown into impact craters may thus control their observed distribution.

[42] Another hypothesis to explain the origin of low-albedo impact crater wall material is that surface type 2 is being eroded and is cascading downward from layers within crater walls, instead of being transported upward. In this scenario, surface type 2 material is indigenous to the crater wall lithology. MOC and MOLA data have been used to show that some crater walls are covered by what appears to be loose, granular material that is at the angle of repose near crater rims [Edgett and Malin, 2000]. Furthermore, outcrops and streaks in crater walls have been observed to run downslope, suggesting that surface type 2 material may be eroding and sliding down the slope surface. The andesite interpretation for surface type 2 would suggest the existence of in-place andesite layers in crater walls. This model is consistent with the Mars Pathfinder conclusion that the material in this region is andesitic in composition [Rieder et al., 1997; McSween et al., 1999].

[43] The weathered basalt interpretation for surface type 2 is also consistent with an indigenous model for material on crater walls. In this scenario, in-place lithologies are altered by sub-aerially emplaced ice and/or water layers and later eroded downwards forming loose material. All material within impact craters is thus originally basalt, as either transported floor material or indigenous wall exposures, with altered basalt forming later and eroding from crater walls. It is uncertain if this type of weathering process is currently altering crater wall surfaces; however, Mars Odyssey Gamma-Ray Spectrometer data [Feldman et al., 2002; Mitrofanov et al., 2002; Boynton et al., 2002] and high-resolution MOC images of pitted and hummocky surfaces [Mustard et al., 2001] suggest the presence of stable near-surface water ice and recent modification of surface materials.

[44] In summary, it is difficult to trace the origin of surface type 1 basalt materials on the floors of impact craters to bedrock exposures because of their mobile nature and eolian origin. It is even more difficult to tie surface type 2 compositions (andesite or weathered basalt) to bedrock exposures because of the uncertainty about whether their sources lie inside or outside the craters, or if they represent local or global source compositions.

### 5.2.2. Low-Albedo Impact Crater Wind Streaks

[45] Several hypotheses exist for the origin of adjacent low-albedo wind streaks. Some models interpret them as resulting from saltation and traction and to consist of sandy material deflated from adjacent dark intracrater deposits [Arvidson, 1974; Thomas, 1984], or to result from material being stripped from the surface to reveal a darker substrate

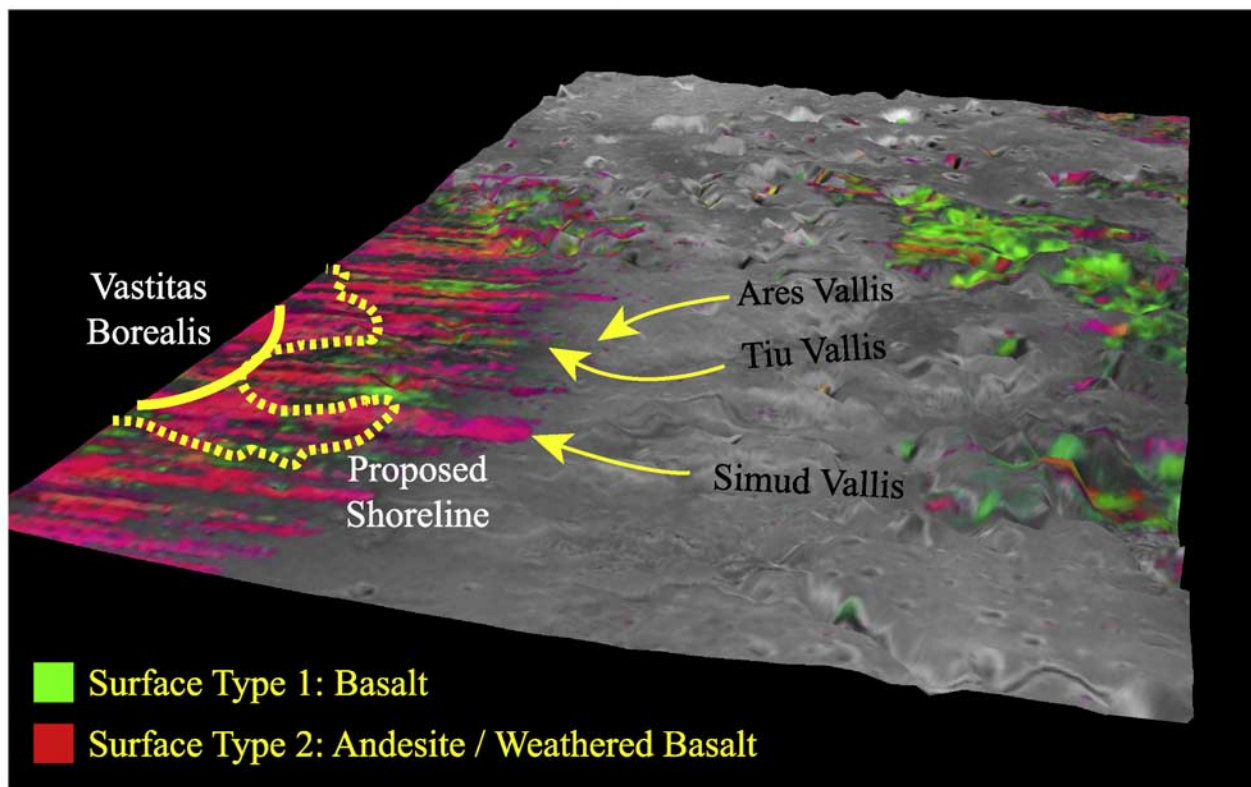


**Figure 11.** Composite MOC, MOLA, and TES map showing the distribution of surface type 1 and type 2 materials in southern Acidalia Planitia and the southern highlands. Arrows indicate the direction of surface type 1 material (basalt) transported in the “dry” model to southern Acidalia Planitia (over indigenous surface type 2 andesite) by large outflow channels in Chryse Planitia. Curved yellow solid line shows extent of the Vastitas Borealis Formation (“wet” deposit model: surface type 2 weathered basalt). Curved yellow dashed line shows geomorphic contacts previously interpreted as ancient shorelines (indigenous coastal marine model: surface type 2 weathered basalt).

[e.g., Soderblom *et al.*, 1978]. Conversely, Thomas and Veverka [1986] proposed that dark wind streaks formed by the deposition of fine dark silt from plumes of suspended material. This view is now supported by MOC observations that suggest the dark materials are mantle deposits of fine-grained sediment deflated from adjacent crater floors, not sand-sized particles [Edgett and Malin, 2000]. Fine-grained particles in wind streaks compared to intracrater material agree with the lack of observed dunes (formed by sand-sized particles) in MOC high-resolution images.

[46] The observation of surface type 1 material grading to surface type 2 material in wind streaks (Figures 5 and 6) may support a combination of depositional and erosional/remnant models. We will first examine the end-members of depositional and erosional models, and then offer a combination model as an alternative.

[47] In a depositional model, both surface type 1 sandy floor material and surface type 2 wall material are deflated from within the crater and deposited to form the wind streak. There are two uncertainties with this model. First, if surface type 1 sandy floor material is deflated out of the crater, why does it not also cover the intervening crater wall observed as surface type 2 material? Second, why are there not dune formations, which form in an eolian environment with sufficient sand supply, in the sandy surface type 1

material in the wind streak? It is thus difficult to account for the observed surface type 1 and type 2 distributions using only a depositional model.

[48] In an erosional model, both surface type 1 and type 2 materials would be locally derived and exposed as overlying material is removed. Uncertainties with this model include how to explain either basalt-andesite or basalt-weathered basalt compositional contacts with no prevailing geologic evidence for different lava flows or different amounts of alteration.

[49] A model that combines deposition and erosion is more consistent with the observed surface type 1 and type 2 distributions in wind streaks. In this model, surface type 2 material is deflated from intracrater walls and deposited on an erosional or protected remnant type 1 surface in the lee of impact craters. Thermal inertia data indicate that particle sizes in the northern extent of wind streaks, where basaltic surfaces are observed, are smaller compared to the sand-sized basaltic particles in intracrater deposits. This may imply that fine-grained surface type 2 materials are mixed with the erosional/remnant surface type 1 materials. This may also explain the less evident mixing trend in wind streaks compared to within impact craters. Remnant material corresponding to surface type 1 basalt would imply a basalt-dominated region, with surface type 2 materials being

locally derived and deflated from within impact craters. Wind streaks may thus result from a combination of processes involving deflation of fine-grained surface type 2 material from intracrater walls that is then deposited on an erosional or protected older remnant of surface type 1 material. This combination model, however, does not provide insight into distinguishing andesite from weathered basalt for surface type 2 compositions.

## 6. Summary

[50] 1. The Oxia Palus quadrangle contains the geographic and compositional transition between the southern highlands and northern lowlands and between surface type 1 and 2 lithologies.

[51] 2. The gradational boundary of surface type 1 and 2 materials in Acidalia and Chryse Planitiae may represent either (1) an influx of basaltic sediment from the southern highlands, deposited on and mixed with andesitic volcanics; (2) an influx of water-transported basaltic sediment from the southern highlands that was altered and later deposited as a thin sedimentary veneer; or (3) different degrees of weathering of basalt marking the geographic extent of submarine alteration of basaltic crust.

[52] 3. Low-albedo intracrater materials grade from surface type 1 to surface type 2 compositions from crater floors upward onto crater walls. The compositional transition coincides with decreasing thermal inertia values that are interpreted to reflect decreasing particle sizes, possibly controlled by mineralogic differences between a largely unweathered basalt component and an andesite/altered basalt component. Intracrater floor materials are interpreted as eolian sediment blown into impact craters. Intracrater wall materials are interpreted as either eolian sediment sorted by particle size or eroded material from in-place crater wall lithologies.

[53] 4. Low-albedo wind streaks display a compositional gradation of surface type 1 to surface type 2 in the direction of wind flow; however, the trend is not as evident as within the impact craters. This distribution may support both deflation and erosional models for the formation of wind streaks.

[54] 5. The Mars Pathfinder landing site and its Ares and Tiu Valles source regions are sufficiently blanketed by fine-grained dust to prohibit the analysis of surface rock compositions. Despite the fact that the MP site is one of the rockiest places on the planet and that dust apparently covers only the upper surfaces of rocks, spectral observations at multiple emission angles remain obscured by dust in the atmosphere.

[55] **Acknowledgments.** We thank T. Hare, J. Bandfield, and V. Hamilton for discussions of the results presented here. We also acknowledge Malin Space Science Systems for use of MGS MOC images. Finally, we would like to thank the TES Engineering, Data Processing and Software teams for all of their outstanding efforts and support.

## References

Aharonson, O., M. T. Zuber, G. A. Neumann, and J. W. Head, Mars: Northern hemisphere slopes and slope distributions, *Geophys. Res. Lett.*, **25**, 4413–4416, 1998.  
 Arvidson, R. E., Wind-blown streaks, splotches, and associated craters on Mars, *Icarus*, **21**, 12–27, 1974.

Bandfield, J. L., Isolation and characterization of Martian atmospheric constituents and surface lithologies using thermal infrared spectroscopy, Ph.D. dissertation, 195 pp., Ariz. State Univ., Tempe, 2000.  
 Bandfield, J. L., P. R. Christensen, and M. D. Smith, Spectral dataset factor analysis and endmember recovery: Application to analysis of Martian atmospheric particulates, *J. Geophys. Res.*, **105**, 9573–9587, 2000a.  
 Bandfield, J. L., V. E. Hamilton, and P. R. Christensen, A global view of Martian surface compositions from MGS-TES, *Science*, **287**, 1626–1630, 2000b.  
 Boynton, W. V., et al., Distribution of hydrogen in the near-surface of Mars: Evidence for sub-surface ice deposits, *Science*, **297**, 81–85, 2002.  
 Christensen, P. R., Eolian intracrater deposits on Mars: Physical properties and global distribution, *Icarus*, **56**, 496–518, 1983.  
 Christensen, P. R., et al., Thermal Emission Spectrometer Experiment: Mars Observer Mission, *J. Geophys. Res.*, **97**, 7719–7734, 1992.  
 Christensen, P. R., J. L. Bandfield, M. D. Smith, V. E. Hamilton, and R. N. Clark, Identification of a basaltic component on the Martian surface from Thermal Emission Spectrometer data, *J. Geophys. Res.*, **105**, 9609–9621, 2000a.  
 Christensen, P. R., et al., Detection of crystalline hematite mineralization on Mars by the Thermal Emission Spectrometer: Evidence for near-surface water, *J. Geophys. Res.*, **105**, 9623–9642, 2000b.  
 Christensen, P. R., et al., The Mars Global Surveyor Thermal Emission Spectrometer experiment: Investigation description and surface science results, *J. Geophys. Res.*, **106**, 23,823–23,872, 2001.  
 Clifford, S. M., and T. J. Parker, The evolution of the Martian hydrosphere: Implications for the fate of a primordial ocean and the current state of the northern plains, *Icarus*, **154**, 40–79, 2001.  
 Crisp, J., and M. J. Bartholomew, Mid-infrared spectroscopy of Pahala Ash palagonite and implications for remote sensing studies of Mars, *J. Geophys. Res.*, **97**, 14,691–14,699, 1992.  
 Edgett, K. S., Low-albedo surfaces and eolian sediment: Mars Orbiter Camera views of western Arabia Terra craters and wind streaks, *J. Geophys. Res.*, **107**(E6), 5038, doi:10.1029/2001JE001587, 2002.  
 Edgett, K. S., and P. R. Christensen, Mars aeolian sand: Regional variations among dark-hued crater floor features, *J. Geophys. Res.*, **99**, 1997–2018, 1994.  
 Edgett, K. S., and P. R. Christensen, Rocks and aeolian features in the Mars Pathfinder landing site region: Viking infrared thermal mapper observations, *J. Geophys. Res.*, **102**, 4107–4200, 1997.  
 Edgett, K. S., and M. C. Malin, New views of Mars eolian activity, materials, and surface properties: Three vignettes from the Mars Global Surveyor Mars Orbiter Camera, *J. Geophys. Res.*, **105**, 1623–1650, 2000.  
 Feldman, W. C., et al., Global distribution of neutrons from Mars: Results from Mars Odyssey, *Science*, **297**, 75–78, 2002.  
 Hamilton, V. E., M. B. Wyatt, H. Y. McSweeney Jr., and P. R. Christensen, Analysis of terrestrial and Martian volcanic compositions using thermal emission spectroscopy: 2. Application to Martian surface spectra from the Mars Global Surveyor Thermal Emission Spectrometer, *J. Geophys. Res.*, **106**, 14,733–14,746, 2001.  
 Head, J. W., H. Heisinger, M. A. Ivanov, M. A. Kreslavsky, S. Pratt, and B. J. Thomson, Possible ancient oceans on Mars: Evidence from Mars Orbiter Laser Altimeter data, *Science*, **286**, 2134–2137, 1999.  
 Head, J. W., M. A. Kreslavsky, and S. Pratt, Northern lowlands of Mars: Evidence for widespread volcanic flooding and tectonic deformation in the Hesperian Period, *J. Geophys. Res.*, **107**(E1), 5003, doi:10.1029/2000JE001445, 2002.  
 Kieffer, H. H., T. Z. Martin, A. R. Peterfreund, B. M. Jakosky, E. D. Miner, and F. D. Palluconi, Thermal and albedo mapping of Mars during the Viking primary mission, *J. Geophys. Res.*, **82**, 4249–4292, 1977.  
 Malin, M. C., and K. S. Edgett, The Mars Global Surveyor Mars Orbiter Camera: Interplanetary cruise through primary mission, *J. Geophys. Res.*, **106**, 23,429–23,570, 2001.  
 Sween, H. Y., Jr., et al., Chemical, multispectral, and textural constraints on the composition and origin of rocks at the Mars Pathfinder landing site, *J. Geophys. Res.*, **104**, 8679–8716, 1999.  
 Mellon, M. T., B. M. Jakosky, H. H. Kieffer, and P. R. Christensen, High-resolution thermal inertia mapping from the Mars Global Surveyor Thermal Emission Spectrometer, *Icarus*, **148**, 437–455, 2000.  
 Mitrofanov, I., et al., Maps of subsurface hydrogen from the high-energy neutron detector, Mars Odyssey, *Science*, **297**, 78–81, 2002.  
 Mustard, J. F., C. D. Cooper, and M. K. Rifkin, Evidence for recent climate change on Mars from the identification of youthful near-surface ground ice, *Nature*, **412**, 411–414, 2001.  
 Parker, T. J., D. S. Gorsline, R. S. Saunders, D. C. Pieri, and D. M. Schneeberger, Coastal geomorphology of the Martian northern plains, *J. Geophys. Res.*, **98**, 11,061–11,078, 1993.  
 Peterfreund, A. R., Visual and infrared observations of wind streaks on Mars, *Icarus*, **45**, 447–467, 1981.

- Presley, M. A., and P. R. Christensen, Thermal conductivity measurements of particulate materials: 2. Results, *J. Geophys. Res.*, *102*, 6551–6566, 1997.
- Ramsey, M. S., and P. R. Christensen, Mineral abundance determination: Quantitative deconvolution of thermal emission spectra, *J. Geophys. Res.*, *103*, 577–596, 1998.
- Rieder, R., et al., The chemical composition of Martian soils and rocks returned by the mobile alpha proton X-ray spectrometer: Preliminary results from the X-ray mode, *Science*, *278*, 1771–1774, 1997.
- Rogers, D., P. R. Christensen, and J. L. Bandfield, Mars volcanic surface compositions: distributions and boundaries examined using multiple orbiter datasets, *Lunar Planet. Sci.* [CD-ROM], *XXXII*, Abstract 2010, 2001.
- Ruff, S. W., and P. R. Christensen, Bright and dark regions on Mars: Particle size and mineralogical characteristics based on Thermal Emission Spectrometer data, *J. Geophys. Res.*, *107*(E12), 5127, doi:10.1029/2001JE001580, 2002.
- Sagan, C., J. Veverka, P. Fox, R. Dubisch, J. Lederberg, E. Levinthall, L. Quam, R. Tucker, J. B. Pollack, and B. A. Smith, Variable features on Mars: Preliminary Mariner 9 television results, *Icarus*, *17*, 346–372, 1972.
- Smith, D. E., et al., Topography of the northern hemisphere of Mars from the Mars Orbiter Laser Altimeter, *Science*, *279*, 1686–1691, 1998.
- Smith, M. D., J. L. Bandfield, and P. R. Christensen, Separation of atmospheric and surface spectral features in Mars Global Surveyor Thermal Emission Spectrometer (TES) spectra, *J. Geophys. Res.*, *105*, 9589–9607, 2000.
- Smith, P. H., et al., Results from the Mars Pathfinder Camera, *Science*, *278*, 1758–1765, 1997.
- Soderblom, L. A., K. Edwards, E. M. Eliason, E. M. Sanchez, and M. P. Charette, Global color variations on the Martian surface, *Icarus*, *34*, 446–464, 1978.
- Tanaka, K. L., The stratigraphy of Mars, *Proc. Lunar Planet. Sci. Conf.*, *17th*, Part 1, *J. Geophys. Res.*, *91*, suppl., E139–E158, 1986.
- Tanaka, K. L., Sedimentary history and mass flow structures of Chryse and Acidalia Planitiae, Mars, *J. Geophys. Res.*, *102*, 4131–4149, 1997.
- Tanaka, K. L., and D. H. Scot, Geologic map of the polar regions of Mars, *U.S. Geol. Surv. Misc. Invest. Ser.*, *Map I-1802-C*, 1987.
- Thomas, P., Martian intracrater splotches: Occurrence, morphology, and colors, *Icarus*, *57*, 205–227, 1984.
- Thomas, P., and J. Veverka, Red/violet contrast reversal on Mars: Significance for eolian sediments, *Icarus*, *66*, 39–55, 1986.
- Thomas, P., J. Veverka, S. Lee, and A. Bloom, Classification of wind streaks on Mars, *Icarus*, *45*, 124–153, 1981.
- Wyatt, M. B., and H. Y. McSween Jr., Weathered basalt as an alternative to andesite, *Nature*, *417*, 263–266, 2002.
- Zuber, M. T., D. E. Smith, S. C. Solomon, D. O. Muhleman, J. W. Head, J. B. Garvin, J. B. Abshire, and J. L. Bufton, The Mars Observer Laser Altimeter investigation, *J. Geophys. Res.*, *97*, 7781–7798, 1992.

---

P. R. Christensen and M. B. Wyatt, Department of Geological Sciences, Mars Space Flight Facility, Arizona State University, Tempe, AZ 85287-6305, USA. (michael.wyatt@asu.edu)

H. Y. McSween Jr. and J. E. Moersch, Department of Geological Sciences, University of Tennessee, Knoxville, TN 37996-1410, USA.